

Observation of Optical and Electrical In-Plane Anisotropy in High-Mobility Few-Layer ZrTe₅

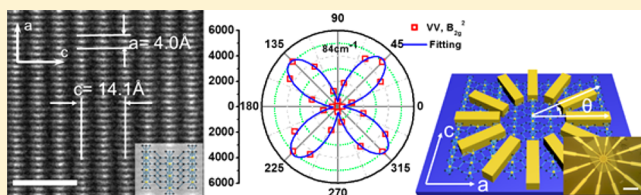
Gang Qiu,^{†,||} Yuchen Du,^{†,||} Adam Charnas,^{†,||} Hong Zhou,^{†,||} Shengyu Jin,^{‡,||} Zhe Luo,^{§,||} Dmitriy Y. Zemlyanov,^{||} Xianfan Xu,^{§,||} Gary J. Cheng,^{‡,||} and Peide D. Ye^{*,†,||}

[†]School of Electrical and Computer Engineering, [‡]School of Industrial Engineering, [§]School of Mechanical Engineering, and ^{||}Birck Nanotechnology Center, Purdue University, West Lafayette, Indiana 47907, United States

S Supporting Information

ABSTRACT: Transition metal pentatelluride ZrTe₅ is a versatile material in condensed-matter physics and has been intensively studied since the 1980s. The most fascinating feature of ZrTe₅ is that it is a 3D Dirac semimetal which has linear energy dispersion in all three dimensions in momentum space. Structure-wise, ZrTe₅ is a layered material held together by weak interlayer van der Waals force. The combination of its unique band structure and 2D atomic structure provides a fertile ground for more potential exotic physical phenomena in ZrTe₅ related to 3D Dirac semimetals. However, the physical properties of its few-layer form have yet to be thoroughly explored. Here we report strong optical and electrical in-plane anisotropy of mechanically exfoliated few-layer ZrTe₅. Raman spectroscopy shows a significant intensity change with sample orientations, and the behavior of angle-resolved phonon modes at the Γ point is explained by theoretical calculations. DC conductance measurement indicates a 50% of difference along different in-plane directions. The diminishing of resistivity anomaly in few-layer samples indicates the evolution of band structure with a reduced thickness. A low-temperature Hall experiment sheds light on more intrinsic anisotropic electrical transport, with a hole mobility of 3000 and 1500 cm²/V·s along the *a*-axis and *c*-axis, respectively. Pronounced quantum oscillations in magnetoresistance are observed at low temperatures with the highest electron mobility up to 44 000 cm²/V·s.

KEYWORDS: ZrTe₅ single crystal, 2D material, optical anisotropy, electrical anisotropy, quantum oscillations



The discovery of graphene¹ began a new era of condensed-matter research because of its unique two-dimensional Dirac band structure, which hosts many profound physical phenomena such as the anomalous integer quantum Hall effect (IQHE).² Since then great efforts have been made toward expanding the spectrum of topological materials and bringing many conceptual materials into reality. Transition metal pentatellurides such as ZrTe₅ and HfTe₅ have been widely studied in bulk form since the early 1980s due to their anomalous resistivity peak and X-ray diffraction intensity peak at low temperature,^{3,4} large thermoelectric power,⁵ pressure-induced superconductivity,^{6,7} absence of a structural phase transition corresponding to resistivity anomaly,⁸ and chiral magnetic effect.⁹ In recent years, ZrTe₅ research has been revived because of its nontrivial topological properties. Some theoretical predictions and experimental results^{10,11} indicate that it is a 3D Dirac semimetal, a mimic of graphene with linear energy dispersion in all three directions. On the other hand, its monolayer form is also claimed to be a candidate of quantum spin Hall insulator,^{12,13} which is very rare among the natural compounds.¹⁴ Shubnikov–de Haas oscillations,^{10,15,16} Zeeman splitting,^{17,18} and fractional quantum Hall effect¹⁹ were also observed in bulk ZrTe₅.

Meanwhile in recent years the 2D family has been expanded to a wide range of materials including narrow bandgap

semiconductors (e.g., black phosphorus^{20,21}), wide bandgap semiconductors (e.g., transition metal dichalcogenides²²), and insulators (e.g., boron nitride²³). Dirac semimetal ZrTe₅ is also a two-dimensional material, with neighboring atomics layer connected by van der Waals force. The interaction of Dirac fermions between interlayers may introduce more exotic physics in this material.

In this Letter, we focus on in-plane anisotropic phenomena of few-layer ZrTe₅, which is a common property shared by a variety of other 2D materials. For example, black phosphorus has electrical²⁰ and thermal²⁴ conductivity anisotropic ratios of around 1.5 and 2, respectively. Black phosphorus also exhibits anisotropic infrared and Raman spectra.²¹ Similar works were carried out on other 2D materials such as graphene²⁵ and TMDs.^{26–28} However, a detailed investigation on anisotropic properties of few-layer ZrTe₅ is still absent. Here we report a systematic study on both optical and electrical anisotropy on few-layer ZrTe₅. The TEM image illustrates the quasi-one-dimensional structure of ZrTe₅, and the strong anisotropy originates from its unique atomic structure. Angle-resolved Raman spectra reveal anisotropic phonon dispersion for

Received: June 25, 2016

Revised: November 16, 2016

Published: November 23, 2016

different Raman modes. This anisotropic Raman behavior is explained by group theory calculation.²⁹ By carefully designing device structures, we find that the DC conductance along the *a*-axis is 1.5 times larger than that along *c*-axis. Finally we carried out a low-temperature Hall experiment to measure carrier concentration and Hall mobility in different directions. Strong Shubnikov–de Haas oscillations were observed in high-mobility ZrTe₅ samples. This work not only gives an insightful understanding of the material anisotropic properties but also provides a reliable means to determine the film orientations.

Figure 1a and b represents the side view and top view of ZrTe₅ lattice structure. One zirconium atom and three

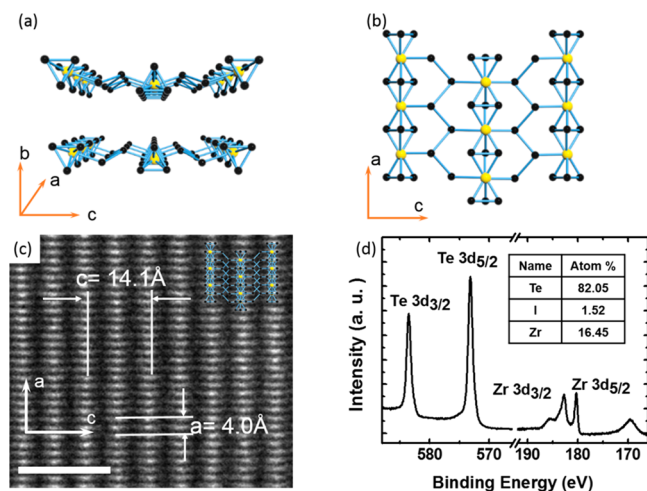


Figure 1. Crystal structure of few-layer ZrTe₅. (a) Perspective side view of few-layer ZrTe₅, (b) top view of monolayer ZrTe₅. (c) Transmission electron microscopy (TEM) image of ZrTe₅ (010) surface. The scale bar is 2 nm. Inset: schematic structure of bilayer ZrTe₅ from (010) surface, which matches the TEM lattice period. (d) X-ray photoemission spectroscopy (XPS) results of binding energies of Zr and Te. The inset table summarizes the atomic ratio of measured sample.

tellurium atoms are arranged into a tetrahedron. These primitives are repeated to form quasi-one-dimensional Zr chains that stretch along the crystalline *a*-axis. Zr atoms in adjacent chains are connected by two Te atoms in distorted angles in *c*-axis to form a 2D layer. The layers are then piled up in *b*-axis with a half-period shift between two neighboring layers. Figure 1c shows the TEM image of (010) surface. The pattern can be interpreted by the inset figure, which is the top view of bilayer structure. Due to the half-period interlayer mismatch, one zirconium atom and four tellurium atoms from adjacent layers form into a unit in TEM structure. Therefore, we can measure the lattice constants from TEM image: *a* = 0.40 nm and *c* = 1.41 nm, which are very close to the results in the literature.^{19,30}

ZrTe₅ bulk crystal was prepared by the vapor transport method. Details of crystal synthesis can be found in Supporting Information. After over 3 weeks of reaction, ZrTe₅ crystal was obtained in the form of clusters of long spikes, with the dimensions on the order of 25 × 1 × 1 mm, as shown in Figure S1a. XPS results (Figure 1d) shows an approximate 1:5 atomic ratio of Zr and Te, with a little trace of transport agent iodine, which may have condensed on the surface of ZrTe₅ during temperature cooling down.

Few-layer ZrTe₅ was exfoliated by Scotch tape and then transferred onto a heavily doped silicon wafer capped with 90 nm SiO₂. Due to the elongated morphology of bulk ZrTe₅ crystal, the exfoliated flakes usually also have slender rectangular shapes. The flake thickness was measured by atomic force microscopy (AFM). Generally speaking, it is difficult to achieve large area of monolayer ZrTe₅ flakes for further study.³¹ Yet we can still find some candidate flakes of three layers or more with appropriate size for fabrication and characterization. Figure S1b displays an AFM image of an exfoliated ZrTe₅ flake with two steps, and the number of layers are identified by AFM to be 2L and 5L respectively.

Angle-resolved Raman spectra were investigated at room temperature. The ZrTe₅ crystal structure belongs to the *Cmcm* (*D*_{2h}¹⁷) space group,³² so there are 12 × 3 vibrational modes at

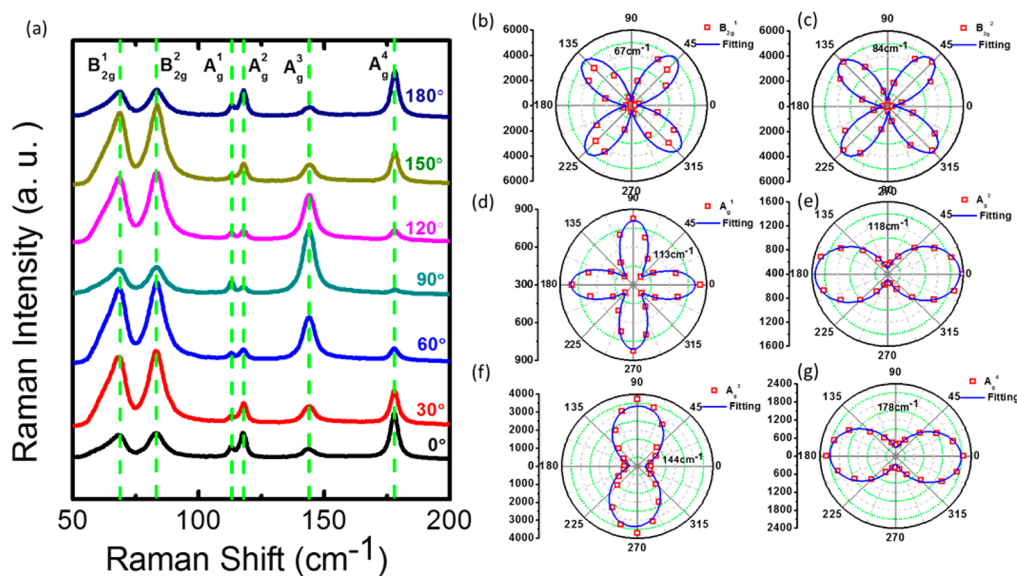


Figure 2. (a) Raman spectra of a fresh exfoliated flake evolving with rotating angle between the flake and incident polarization. (b–g) are corresponding to *B*_{2g}¹, *B*_{2g}², *A*_g¹, *A*_g², *A*_g³, and *A*_g⁴ Raman modes which are located at 67, 84, 113, 118, 144, and 178 cm⁻¹. The fitted curves are described as eq 3 and 4.

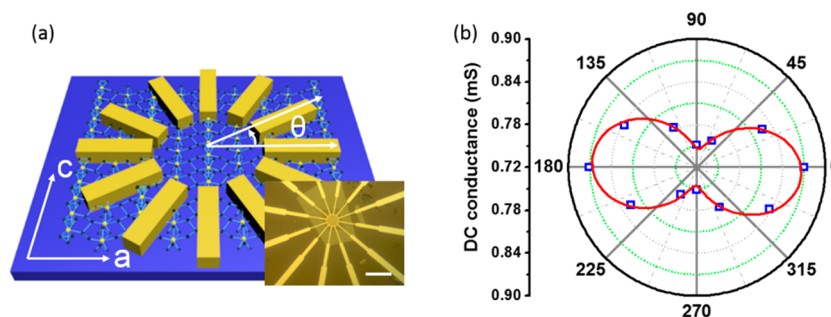


Figure 3. Angle-resolved DC conductance measurements on ZrTe_5 flake. (a) Schematic view of device structure. Inset: optical image of a real device. Scale bar is $10 \mu\text{m}$. (b) Angle-dependent DC conductance. The data points are fitted with the equation: $\sigma_\theta = \sigma_x \sin^2\theta + \sigma_y \cos^2\theta$.

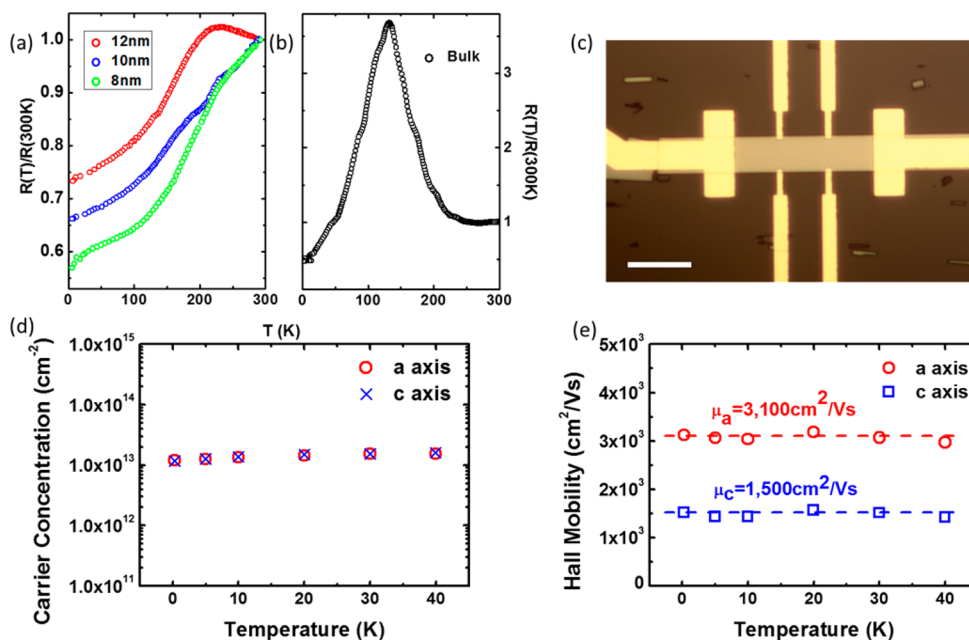


Figure 4. Low-temperature transport measurements. Resistivity vs temperature curve on (a) few-layer and (b) bulk ZrTe_5 samples. The resistivity is normalized based on room temperature values. (c) Optical image of the Hall-bar device. The scale bar is $10 \mu\text{m}$. Temperature dependence of (d) carrier concentration and (e) Hall mobility along two principal axis.

the Γ point of Brillouin zone, among which 18 are Raman-active.^{33–35} Two B_{2g} modes and six A_g modes are predicted to be observable when the laser shines perpendicular to (010) surface according to previous study.^{33,34} In our experiment, one of the A_g modes is out of the Raman system detector range (39 cm^{-1}), and another one is relatively weak at room temperature (235 cm^{-1}), so we focus on the remaining six peaks located at $67, 84, 113, 118, 144,$ and 178 cm^{-1} . Freshly exfoliated thin ZrTe_5 flakes were transferred onto a Si substrate and then mounted onto a rotation stage. Raman spectra were excited by 633 nm He–Ne laser which was incident along b -axis and polarized parallel to a -axis. A linear polarizer was placed in front of spectrometer. Only the scattered phonons aligned with polarizer direction can pass through and be collected by the detector. In our experiment, the polarizer is first placed parallel to the incident photon polarization, which is denoted as the ac(aa)ac configuration, since this configuration gives the maximum Raman signal. Figure 2a presents Raman spectra of ZrTe_5 evolving with angles in this configuration. The intensity of six major peaks are extracted and plotted into polar figures in Figure 2b–g. In the meantime, the results of ac(ac)ac configuration (polarizer is perpendicular to the incident light) is also reported in the Supporting Information.

The intensity of different Raman vibration modes can be described as²⁹

$$I = |\mathbf{e}_i \times \mathbf{R} \times \mathbf{e}_s|^2 \quad (1)$$

where \mathbf{e}_i is the unit vector of incident laser polarization and \mathbf{e}_s stands for the scattering phonon polarization. \mathbf{R} is the Raman tensor for a certain vibration mode. Here we assign the angle between incident laser polarization and a -axis of the lattice of ZrTe_5 to be θ . In the ac(aa)ac configuration, \mathbf{e}_i is parallel to \mathbf{e}_s ; thus both of them can be written as $\mathbf{e}_i = \mathbf{e}_s^T = (\cos \theta, 0, \sin \theta)$. The Raman tensor can be for A_g and B_{2g} modes are²⁴

$$\mathbf{R}_{A_g} = \begin{pmatrix} A & & \\ & B & \\ & & C \end{pmatrix} \quad \mathbf{R}_{B_{2g}} = \begin{pmatrix} & & E \\ & & \\ E & & \end{pmatrix} \quad (2)$$

Back substituting into eq 1, for the ac(aa)ac configuration, we have

$$I_{A_g} = (A \cos^2\theta + C \sin^2\theta)^2 \quad (3)$$

$$I_{B_{2g}} = E^2 \sin^2 2\theta \quad (4)$$

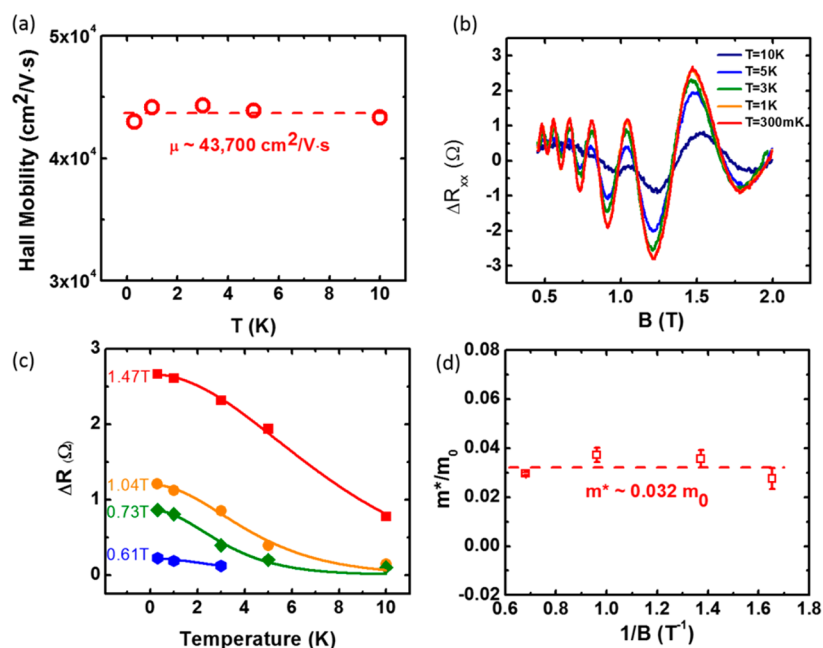


Figure 5. (a) Hall mobility extracted from the slope of R_{xy} . (b) SdH quantum oscillations as a function of the B field after subtracting from a smooth background. (c) Temperature dependence of oscillation amplitudes. (d) Effective mass versus $1/B$ extracted from panel c using eq 5.

The fitted curve based on the calculations are in good agreement with the experimental data. It is straightforward to understand the results for B_{2g} modes (Figure 2b–c), since both of them have four branches, with maxima and minima at 45° and 90°. In case of A_g^1 modes (Figure 2d), $A = -C$ gives the period of 90° and maxima at 0°. The rest three modes have only two branches, indicating one of the constants in eq 3 has to be zero. A_g^2 and A_g^4 mode plots are fitted with $C = 0$, and A_g^3 is fitted with $A = 0$.

To investigate the electrical anisotropy of ZrTe_5 , we measured angle-resolved DC conductance. Knowing the fact that the growth rate in a -axis is much faster than b - and c -axes, we can preliminarily determine the flake orientation by assigning the long edge of rectangular shape to the a -axis. Then we use Raman spectrum to further verify the lattice orientation by the aforementioned method. Prior to fabrication, the flakes were trimmed into circles with the diameter of 10 μm by BCl_3/Ar based dry etching. After patterning we can eliminate the nonideal geometric factors that might be influential on the current flow. Twelve contacts were patterned by electron-beam lithography (EBL) and arranged in a circle concentric with the etched flakes in different orientations. The interval between two neighboring contacts are 30° and 0° is aligned with a -axis. 30 nm Ni and 50 nm Au metal were deposited by electron-beam evaporator. Figure 3a schematically illustrates the structure of the device, and the inset of Figure 3a is an optical image of the real device. DC conductance was measured between each pair of diagonal contacts as zero back gate bias. A 20% disparity of DC conductance is observed from different angles, as shown in Figure 3b. Low-field conductivity of an anisotropic material at a certain angle θ can be decomposed into two orthogonal components:¹⁹ $\sigma_\theta = \sigma_x \sin^2\theta + \sigma_y \cos^2\theta$, where σ_x is the conductivity along (100) direction and σ_y is the conductance along (001) direction. Angle-resolved DC conductance measurement reveals the anisotropic transport properties; nevertheless this circular structure underestimates the anisotropic ratio of mobility,

which is a fundamental material property, because of fringing current along the conducting path counteracting against anisotropic transport. By designing a more refined L-shaped structure (see Supporting Information), we accurately measured the DC conductance ratio along two primary in-plane axis to be ~ 1.5 .

To acquire more intrinsic understanding of transport properties, we performed low-temperature transport experiments. One of the trademarks of ZrTe_5 transport is the anomalous resistivity peak at around 130 K (Figure 4b). By reducing the temperature, the ZrTe_5 bulk sample undergoes an anomalous resistivity peak, along with the changing sign of Hall coefficient and thermoelectric power.³² For decades the origin of resistivity peak is under debate and still elusive. Some popular explanation includes formation of charge density waves,³⁶ temperature-induced band movement,¹¹ polaronic behavior,³⁷ and structural phase transition.³⁸ So far no direct experimental evidence can support any of the proposals. We explored the anomalous resistivity behavior in few-layer ZrTe_5 samples. By reducing the flake thickness, the resistivity peak gradually attenuated and eventually disappeared. For thin samples under 10 nm, resistivity reduces with temperature monotonically in the full temperature range, as shown in Figure 4a. Similar results has also been observed in other publications.³¹ The Fermi surface of ZrTe_5 is complicated, where an electron pocket and a hole pocket contributes to the transport simultaneously. Thus, the vanishing of resistivity peak is reckoned as an implication of band structure evolution from bulk to few-layer samples. In bulk sample, the Fermi level gradually moves up as temperature drops, so it exhibits a transition from hole-dominant region to electron-dominant region, along with the resistivity peak. Whereas in few-layer sample, the bandgap increased due to reduced flake thickness, and electron and hole pockets are no longer entangled together which simplifies the scenario; therefore, the R – T curve shows monotonous change.³¹

On the other hand magneto transport experiment is conducted to measure the carrier concentration and Hall mobility along different directions at low-temperature. Standard six-terminal Hall-bar samples (Figure 4c) were fabricated with either *a*-axis or *c*-axis in the longitude direction. The thickness of the devices is ~ 30 nm. Hall mobility and carrier concentrations are obtained by measuring longitudinal resistivity ρ_{xx} and Hall resistivity ρ_{xy} at low temperatures and external magnetic fields. The complexity of the Fermi surface makes it difficult to extract mobility and carrier density, since Hall resistivity displays anomalous behavior with both negative and positive slopes (Figure S5a). The appropriate methods to extract Hall mobility and carrier density would be to apply the two-carrier model. We attempted to extract mobility and carrier density of the dominant carrier type with a simplified method by extracting from the slope of near-linear large *B*-field region (Figure S5b). A discussion on the correctness of the simplified method as well as comparison of these two methods can be found in Supporting Information. Figure 4d and e shows temperature-dependent hole concentration and Hall mobility along two directions. While the carrier concentrations remain the same along two directions, a significant difference arises from Hall mobility. The hole mobility along the *a*-axis is ~ 3000 $\text{cm}^2/\text{V}\cdot\text{s}$ and along the *c*-axis is ~ 1500 $\text{cm}^2/\text{V}\cdot\text{s}$, which is around a factor of 2 difference.

Particularly worth mentioning is in a 23 nm thick sample electrons become the dominant carrier type and electron Hall mobility reaches over $44\,000$ $\text{cm}^2/\text{V}\cdot\text{s}$ along the *a*-axis and strong Shubnikov–de Haas (SdH) oscillations are well developed under 10 K as shown in Figure 5b. The SdH oscillations commence around small *B*-field around 0.3 T (see inset of Figure S5c), hence according to observability criteria of SdH oscillations, we can estimate the electron mobility: $\mu_e > 10^4/B \approx 33\,000$ $\text{cm}^2/\text{V}\cdot\text{s}$, which is a reasonable approximation to the value we extracted from R_{xy} . The inconsistency of Hall resistivity behavior in different samples was presumed to arise from the thickness-induced bandgap widening, and two types of carriers are disentangled at the Fermi surface. More details are discussed in Supporting Information. Hall mobility is extracted from Hall resistivity curve and plotted in Figure 5a. By subtracting a smooth background, SdH oscillation amplitude ΔR_{xx} (Figure 5b) is obtained. Oscillation amplitude versus temperature at different *B*-fields (Figure 5c) are fitted by the Lifshitz–Kosevich equation:³⁹

$$\Delta R_{xx} \propto \frac{2\pi^2 k_B m^* T / \hbar e B}{\sinh(2\pi^2 k_B m^* T / \hbar e B)} \quad (5)$$

from which we can extract the effective mass to be $\sim 0.032m_0$ (Figure 5d). The extracted effective mass is $0.032m_0$, which is very close to the results in other works.^{10,16,17,19}

In summary, we synthesized bulk ZrTe_5 single crystal by the vapor transport method and mechanically peeled it down to few-layer flakes. We applied XPS to confirm the elementary composition and TEM image to elucidate the lattice structure. Raman spectroscopy reveals different phonon dispersion modes at the Γ points, and the angle-resolved peak intensity behavior is in good agreement with calculations. We also measured DC conductance along different axis with a significant anisotropic ratio of around 1.5 at room temperature. The anomalous resistivity peak at low temperature vanished in few-layer samples, which implies the disentanglement of hole pocket and electron pocket at Fermi surface resulting from bandgap

widening as thickness reduces. Finally we carried out Hall measurements at low temperatures to provide an insightful perspective of anisotropic transport. Hall mobility along *a*- and *c*-axes are 3000 and 1500 $\text{cm}^2/\text{V}\cdot\text{s}$, respectively. SdH oscillations were observed in the sample where the electron mobility reaches up to $44\,000$ $\text{cm}^2/\text{V}\cdot\text{s}$. The strong optical and electrical anisotropy not only gives us a detailed understanding of this material system but also offers a solid method to determine crystal orientation.

■ ASSOCIATED CONTENT

Supporting Information

The Supporting Information is available free of charge on the ACS Publications website at DOI: [10.1021/acs.nanolett.6b02629](https://doi.org/10.1021/acs.nanolett.6b02629).

Details of crystal growth, few-layer AFM image, additional optical and electrical results, device fabrication, discussion of Hall resistivity and mobility extraction, and two carrier model (PDF)

■ AUTHOR INFORMATION

Corresponding Author

*E-mail: yep@purdue.edu. Fax: 765-496-7443.

ORCID

Zhe Luo: 0000-0002-8129-333X

Gary J. Cheng: 0000-0002-1184-2946

Peide D. Ye: 0000-0001-8466-9745

Notes

The authors declare no competing financial interest.

■ ACKNOWLEDGMENTS

One of the authors (P.D.Y.) would like to thank W. Pan and Z. Jiang for the valuable discussion, which initiates this research work. This material is based upon work partly supported by AFOSR/NSF EFRI 2-DARE Grant No. 1433459-EFMA and partly supported by SRC GRC program. The low-temperature measurements were performed at the National High Magnetic Field Laboratory (NHMFL), which is supported by National Science Foundation Cooperative Agreement No. DMR-1157490, the State of Florida, and the U.S. Department of Energy. The authors would like to thank T. Murphy, J.-H. Park, G. Jones, Z. Wan, Y. Wang, and L. Rokhinson for experimental assistance.

■ REFERENCES

- (1) Geim, A. K.; Novoselov, K. S. *Nat. Mater.* **2007**, *6*, 183–191.
- (2) Zhang, Y. B.; Tan, Y. W.; Stormer, H. L.; Kim, P. *Nature* **2005**, *438*, 201–204.
- (3) Skelton, E. F.; Wieting, T. J.; Wolf, S. a.; Fuller, W. W.; Gubser, D. U.; Francavilla, T. L.; Levy, F. *Solid State Commun.* **1982**, *42*, 1–3.
- (4) Tritt, T.; Lowhorn, N.; Littleton, R.; Pope, A.; Feger, C.; Kolis, J. *Phys. Rev. B: Condens. Matter Mater. Phys.* **1999**, *60*, 7816–7819.
- (5) Jones, T. E.; Fuller, W. W.; Wieting, T. J.; Levy, F. *Solid State Commun.* **1982**, *42*, 793–798.
- (6) Zhou, Y.; Wu, J.; Ning, W.; Li, N.; Du, Y.; Chen, X.; Zhang, R.; Chi, Z.; Wang, X.; Zhu, X.; Lu, P.; Ji, C.; Wan, X.; Yang, Z.; Sun, J.; Yang, W.; Tian, M.; Zhang, Y.; Mao, H. *Proc. Natl. Acad. Sci. U. S. A.* **2016**, *113*, 2904–2909.
- (7) Liu, Y.; Long, Y. J.; Zhao, L. X.; Nie, S. M.; Zhang, S. J.; Weng, Y. X.; Jin, M. L. *arXiv* **2016**, 1603.00514.
- (8) Bullett, D. W. *Solid State Commun.* **1982**, *42*, 691–693.

- (9) Li, Q.; Kharzeev, D. E.; Zhang, C.; Huang, Y.; Pletikosić, I.; Fedorov, A. V.; Zhong, R. D.; Schneeloch, J. A.; Gu, G. D.; Valla, T. *Nat. Phys.* **2016**, *12*, 1–6.
- (10) Zheng, G.; Lu, J.; Zhu, X.; Ning, W.; Han, Y.; Zhang, H.; Zhang, J.; Xi, C.; Yang, J.; Du, H.; Yang, K.; Zhang, Y.; Tian, M. *Phys. Rev. B: Condens. Matter Mater. Phys.* **2016**, *93*, 1–7.
- (11) Zhang, Y.; Wang, C.; Yu, L.; Liu, G.; Liang, A.; Huang, J.; Nie, S.; Zhang, Y.; Shen, B.; Liu, J.; Weng, H.; Zhao, L.; Chen, G.; Jia, X.; Hu, C.; Ding, Y.; He, S.; Zhao, L.; Zhang, F.; Zhang, S.; Yang, F.; Wang, Z.; Peng, Q.; Dai, X.; Fang, Z.; Xu, Z.; Chen, C.; Zhou, X. *J. arXiv* **2016**, 1602.03576.
- (12) Weng, H.; Dai, X.; Fang, Z. *Phys. Rev. X* **2014**, *4*, 1–8.
- (13) Wu, R.; Ma, J.-Z.; Nie, S.-M.; Zhao, L.-X.; Huang, X.; Yin, J.-X.; Fu, B.-B.; Richard, P.; Chen, G.-F.; Fang, Z.; Dai, X.; Weng, H.-M.; Qian, T.; Ding, H.; Pan, S. H. *Phys. Rev. X* **2016**, *6*, 021017.
- (14) Ando, Y. *J. Phys. Soc. Jpn.* **2013**, *82*, 1–32.
- (15) Izumi, M.; Nakayama, T.; Uchinokura, K.; Harada, S.; Yoshizaki, R.; Matsuura, E. *J. Phys. C: Solid State Phys.* **1987**, *20*, 3691–3705.
- (16) Yuan, X.; Zhang, C.; Liu, Y.; Song, C.; Shen, S.; Sui, X.; Xu, J.; Yu, H.; An, Z.; Zhao, J.; Yan, H.; Xiu, F. *arXiv* **2015**, 1510.00907.
- (17) Liu, Y.; Yuan, X.; Zhang, C.; Jin, Z.; Narayan, A.; Luo, C.; Chen, Z.; Yang, L.; Zou, J.; Wu, X.; Sanvito, S.; Xia, Z.; Li, L.; Wang, Z.; Xiu, F. *Nat. Commun.* **2016**, *7*, 12516.
- (18) Zheng, G.; Zhu, X.; Lu, J.; Ning, W.; Zhang, H.; Gao, W.; Han, Y.; Yang, J.; Du, H.; Yang, K.; Zhang, Y. *arXiv* **2016**, 1607.05384.
- (19) Yu, W.; Jiang, Y.; Yang, J.; Dun, Z. L.; Zhou, H. D.; Jiang, Z.; Lu, P.; Pan, W. *arXiv* **2016**, 1602.06824.
- (20) Liu, H.; Neal, A.; Zhu, Z.; Luo, Z.; Xu, X.; Tomanek, D.; Ye, P. D. *ACS Nano* **2014**, *8*, 4033–4041.
- (21) Xia, F.; Wang, H.; Jia, Y. *Nat. Commun.* **2014**, *5*, 4458.
- (22) Radisavljevic, B.; Radenovic, A.; Brivio, J.; Giacometti, V.; Kis, A. *Nat. Nanotechnol.* **2011**, *6*, 147–150.
- (23) Watanabe, K.; Taniguchi, T.; Kanda, H. *Nat. Mater.* **2004**, *3*, 404–409.
- (24) Luo, Z.; Maassen, J.; Deng, Y.; Du, Y.; Lundstrom, M. S.; Ye, P. D.; Xu, X. *Nat. Commun.* **2015**, *6*, 1–32.
- (25) Park, C.-H.; Yang, L.; Son, Y.-W.; Cohen, M. L.; Louie, S. G. *Nat. Phys.* **2008**, *4*, 213–217.
- (26) Wolverson, D.; Crampin, S.; Kazemi, A. S.; Ilie, A.; Bending, S. J. *ACS Nano* **2014**, *8*, 11154–11164.
- (27) Zhao, S.; Wang, H.; Zhou, Y.; Liao, L.; Jiang, Y.; Yang, X.; Chen, G.; Lin, M.; Wang, Y.; Peng, H.; Liu, Z. *Nano Res.* **2015**, *8*, 288–295.
- (28) Lin, Y. C.; Komsa, H. P.; Yeh, C. H.; Björkman, T.; Liang, Z. Y.; Ho, C. H.; Huang, Y. S.; Chiu, P. W.; Krasheninnikov, A. V.; Suenaga, K. *ACS Nano* **2015**, *9*, 11249–11257.
- (29) Zhao, Y.; Luo, X.; Li, H.; Zhang, J.; Araujo, P. T.; Gan, C. K.; Wu, J.; Zhang, H.; Quek, S. Y.; Dresselhaus, M. S.; Xiong, Q. *Nano Lett.* **2013**, *13*, 1007–1015.
- (30) Fjellvag, H.; Kjekshus, A. *Solid State Commun.* **1986**, *60*, 91–93.
- (31) Niu, J.; Wang, J.; He, Z.; Zhang, C.; Li, X.; Cai, T.; Ma, X.; Jia, S.; Yu, D.; Wu, X. *arXiv* **2015**, 1511.09315.
- (32) Kamm, G. N.; Gillespie, D. J.; Ehrlich, A. C.; Wieting, T. J.; Levy, F. *Phys. Rev. B: Condens. Matter Mater. Phys.* **1985**, *31*, 7617–7623.
- (33) Taguchi, I.; Grisel, A.; Levy, F. *Solid State Commun.* **1983**, *46*, 299–303.
- (34) Fallis, A. J. *Chem. Inf. Model.* **1984**, *53*, 1689–1699.
- (35) Zwick, A.; Landa, G.; Carles, R.; Renucci, M. A.; Kjekshus, A. *Solid State Commun.* **1982**, *44*, 89–94.
- (36) Okada, S.; Sambongi, T.; Ido, M.; Tazuke, Y.; Aoki, R.; Fujita, O. *J. Phys. Soc. Jpn.* **1982**, *51*, 460–467.
- (37) Rubinstein, M. *Phys. Rev. B: Condens. Matter Mater. Phys.* **1999**, *60*, 1627.
- (38) DiSalvo, F. J.; Fleming, R. M.; Waszczak, J. V. *Phys. Rev. B: Condens. Matter Mater. Phys.* **1981**, *24*, 2935.
- (39) Novoselov, K. S.; Geim, A. K.; Morozov, S. V.; Jiang, D.; Katsnelson, M. I.; Grigorieva, I. V.; Dubonos, S. V.; Firsov, A. A. *Nature* **2005**, *438*, 197–200.